Received: 5 November 2023 | Revised: 30 January 2024 | Accepted: 12 February 2024

DOI: 10.1002/eom2.12440

RESEARCH ARTICLE

EcoMat FUNCTIONAL MATERIALS FOR GREEN ENERGY AND ENVIRONMENT WILEY

Semi-transparent metal electrode-free all-inorganic perovskite solar cells using floating-catalyst-synthesized carbon nanotubes

Saemon Yoon[1] | **Il Hyun Lee**[2] | **Jiye Han**[2] | **Jitendra Bahadur**[1] | **Seojun Lee**[1] | **Sangsu Lee**[2] | **Dong Suk Kim**[3] | **B. Mikladal**[4] | **Esko I. Kauppinen**[5] | **Dong-Won Kang**[6] | **Il Jeon**[2]

[1]Department of Smart Cities, Chung-Ang University (CAU), Seoul, Republic of Korea

[2]Department of Nano Engineering, Department of Nano Science and Technology, SKKU Advanced Institute of Nanotechnology (SAINT), Sungkyunkwan University (SKKU), Suwon, Republic of Korea

[3]Energy and Chemical Engineering, Ulsan National Institute of Science and Technology (UNIST), Ulsan, Republic of Korea

[4]Canatu, Ltd., Helsinki, Finland

[5]Department of Applied Physics, Aalto University School of Science, Aalto, Finland

[6]School of Energy Systems Engineering, Chung-Ang University (CAU), Seoul, Republic of Korea

Correspondence
Il Jeon, Department of Nano Engineering, Department of Nano Science and Technology, SKKU Advanced Institute of Nanotechnology (SAINT), Sungkyunkwan University (SKKU), Suwon 16419, Republic of Korea.
Email: il.jeon@spc.oxon.org

Dong-Won Kang, School of Energy Systems Engineering, Chung-Ang University (CAU), Seoul 06974, Republic of Korea.
Email: kangdwn@cau.ac.kr

Funding information
Ministry of Science and ICT (MSIT) of Korea, Grant/Award Numbers: NRF-2023R1A2C3007358, RS-2023K2A9A2A23000283, RS-2023-00217270, RS-2023-00212744

Abstract

Perovskite solar cells offer a promising future for next-generation photovoltaics owing to numerous advantages such as high efficiency and ease of processing. However, two significant challenges, air stability, and manufacturing costs, hamper their commercialization. This study proposes a solution to these issues by introducing a floating catalyst-based carbon nanotube (CNT) electrode into all-inorganic perovskite solar cells for the first time. The use of CNT eliminates the need for metal electrodes, which are primarily responsible for high fabrication costs and device instability. The nanohybrid film formed by combining hydrophobic CNT with polymeric hole-transporting materials acted as an efficient charge collector and provided moisture protection. Remarkably, the metal-electrode-free CNT-based all-inorganic perovskite solar cells demonstrated outstanding stability, maintaining their efficiency for over 4000 h without encapsulation in air. These cells achieved a retention efficiency of 13.8%, which is notable for all-inorganic perovskites, and they also exhibit high transparency in both the visible and infrared regions. The obtained efficiency was the highest for semi-transparent all-inorganic perovskite solar cells. Building on this, a four-terminal tandem device using a low-band perovskite solar cell achieved a power conversion efficiency of 21.1%. These CNT electrodes set new

Saemon Yoon and Il Hyun Lee contributed equally to this study.

benchmarks for the potential of perovskite solar cells with groundbreaking device stability and tandem applicability, demonstrating a step toward industrial applications.

KEYWORDS

carbon electrode, carbon nanotube, floating catalyst, inorganic perovskite solar cell, metal-free electrode

1 | INTRODUCTION

Since their advent in 2009, organic–inorganic lead-halide perovskite solar cells (PSCs) have attracted significant scholarly attention as a promising class of next-generation thin-film photovoltaic devices.[1–3] These solar cells exhibit high power conversion efficiency (PCE), relatively low material costs, and lend themselves to facile solution processing methods.[4–7] Nevertheless, several key hurdles, such as the issues of device stability and manufacturing costs, must be overcome before they can be commercially viable.[8–10] The issue of PSC stability predominantly arises from the use of organic components in the perovskite active layer and the susceptibility of perovskite crystals to moisture and ion migration.[11] Perovskite crystals in PSCs are represented by the chemical formula ABX_3, where A and B represent organic and metal cations, respectively, and X represents a halide anion.[12–15] The organic cation A within the perovskite structure readily absorbs water from the environment,[16–18] resulting in water molecules penetrating the perovskite crystal lattice upon exposure to air. This disrupts the orderly arrangement of ions and triggers hydrolysis reactions, thus compromising the integrity of the crystal. Simultaneously, perovskite materials exhibit a predisposition toward ion migration.[19,20] This phenomenon involves ions moving within the crystal lattice.[21,22] Typical PSCs incorporate metal electrodes that are deposited using thermal evaporation under vacuum conditions, a process that inadvertently encourages metal ion migration into the perovskite layer.[23–25] This migration induces localized alterations in the material composition, defect formation, and expedited degradation of the perovskite material. In addition, the employment of metal electrodes via thermal evaporation in vacuum substantially increases the overall manufacturing costs. In addition to the cost of the deposition process, inert metal sources, such as gold and silver, are costly, which hinders the commercialization of PSCs. Given these considerations, replacing the organic components of the perovskite active material and metal electrodes used in PSCs is crucial.[26,27] Such advancements would address the pivotal challenge of device stability while simultaneously leveraging the low-cost benefits intrinsic to PSCs.[28]

Researchers have pioneered the development of all-inorganic PSCs to substitute organic A-site cations.[29] All-inorganic perovskites using Cs^+ as the A-site cation ($CsPbI_xBr_{3-x}$, where x ranges from 0 to 3) exhibit remarkable thermal and ambient stabilities when integrated into PSCs. While $CsPbI_3$ possesses an appropriate band gap of ~1.73 eV, the active α-$CsPbI_3$ black inorganic perovskite phase is susceptible to a phase transition to the unwanted yellow δ-phase.[30,31] In the case of $CsPbBr_3$, it exhibits remarkable phase stability despite an unnecessarily wide bandgap of 2.36 eV.[32] Therefore, mixed-halide-based all-inorganic perovskite compositions, $CsPbI_2Br$ (CPIB), were used in this study, showing high photovoltaic performance and stability. In addition, it holds promise for the development of efficient single-junction PSCs and tandem solar cells (TSCs) owing to its appropriate band gap (1.91 eV).[33–38] Although initially constrained by a low PCE, concerted international research endeavors successfully increased the PCE to 18.05%.[39] Recently reported CPIB PSCs demonstrated device stability times exceeding 1000 h under ambient conditions, even without encapsulation.[40–43] This is a significant advancement compared to organic–inorganic PSCs, which typically demonstrate stability between 100 and 300 h.[44–48] Further enhancement of all-inorganic PSCs can be achieved by replacing the top metal electrode with hydrophobic carbon electrodes, which inhibit moisture penetration and metal ion migration.[49–52] Moreover, because carbon electrodes are composed exclusively of carbon atoms, they can significantly reduce fabrication costs and offer a solution for raw material shortages.[53–55] Furthermore, the introduction of semi-transparent carbon electrodes enables the tandem application of CPIB PSCs, further augmenting their PCE.

To date, two mainstream carbon electrodes have been used as top electrodes in PSCs: paste-type and film-type carbon nanotube (CNT) electrodes.[56–60] The first paste-type carbon electrode in PSCs was reported by Han et al.[61] This type of carbon electrode exhibits high PCE, and the highest PCEs recorded are 18.1% for organic–inorganic PSCs and 15.56% for all-inorganic PSCs.[62,63] However, the paste-type carbon electrodes necessitate high-temperature thermal curing above 500°C, which

limits the feasibility of flexible device applications. In addition, the electrodes are nontransparent, and tandem applications are not possible. Additionally, the microscale thickness of such electrodes results in a large, and hence inefficient, pitch distance when fabricating solar modules. Importantly, these carbon electrodes demonstrate lower PCEs than traditional metal electrode-based PSCs due to their inferior hole extraction efficiency and electrical conductivity. Conversely, film-type CNT electrodes fabricated using the floating-catalyst chemical vapor deposition (FCCVD) method exhibit higher PCEs when used as top electrodes in PSCs while possessing the advantages of being semi-transparent and nanometer-scale thin and facile processability at room temperature.[64] Since their initial report, organic–inorganic PSCs incorporating FCCVD-synthesized CNT top electrodes have shown high PCEs, with the current highest recorded value of 20.25%.[65–71] This remarkable performance is attributed to the nanoporous CNT network, which allows the nanohybrid formation of CNT with hole-transporting materials (HTM), thereby significantly improving the hole extraction efficiency. In addition to their high PCE, the semi-transparent nature of the FCCVD-synthesized film-type CNTs extends their potential applications to TSCs and building-integrated photovoltaics (BIPV).[72–77] Moreover, dry and direct transferability offers a distinct advantage over other carbon electrodes, particularly roll-to-roll processability. The application of CNT electrodes in metal-electrode-free PSCs has only been reported in organic–inorganic perovskite systems. Therefore, all-inorganic PSCs remain unexplored, demanding an urgent investigation of their compatibility and performance.

In this study, all-inorganic PSCs were fabricated using FCCVD-synthesized CNT electrodes. These CNT-laminated, metal electrode-free, all-inorganic PSCs were semi-transparent, with a transmittance of ca. 80% at a wavelength of 550 nm. Fabricated using this method, the devices showed a PCE of 13.8% and unprecedented device stability exceeding 4000 h under ambient conditions (25°C, relative humidity of 15%), even without encapsulation. Notably, the efficiency attained was the highest among all reported semi-transparent carbon-based all-inorganic PSCs. This extraordinary performance in terms of efficiency and stability is attributed to the increased concentration of the hole-transporting polymer, poly(3-hexylthiophene-2,5-diyl) (P3HT). A distinctive advantage of FCCVD-synthesized CNT-based PSCs is that the HTM was deposited after the lamination of the CNT electrode. This unorthodox sequence of operations enables the use of a higher HTM concentration. This, in turn, leads to an elevated hole extraction coefficient and provides an improved moisture barrier. Capitalizing on the semitransparent trait, a remarkable 21.1% efficiency was achieved through its tandem application with Sn–Pb PSCs, which absorb light at wavelengths longer than 660 nm.

2 | RESULTS AND DISCUSSION

CNT electrodes were synthesized using the FCCVD method, as depicted in Figure S1. The resulting CNT films exhibited a high transmittance across the visible and near-infrared regions, suggesting their potential for tandem applications and BIPV when employed as top electrodes in PSCs (Figure S2). In terms of conductivity, FCCVD-synthesized CNT electrodes have a distinct advantage over other carbon-based electrodes such as graphite, graphene, and conventional CNTs.[64,67,68] This is because of their high electrical conductivities in all directions, as opposed to the direction-specific conductivities observed in most carbon electrodes (Figure 1A). Relatively long tube lengths, uniform diameters, and minimal bundles resulted in high conductivity. Furthermore, the nanoporous CNT network enabled the formation of a nanohybrid film via intercalation with HTMs, which was subsequently applied to the lamination of the CNT electrode. This configuration ensures a significantly enhanced hole-extraction coefficient and provides superior protection against moisture and oxygen compared to other carbon electrode-based PSCs.[78] Another notable feature of the FCCVD-synthesized CNT electrodes is their nanometer-scale thinness, which ensures a higher PCE for large-sized modules owing to a reduced pitch (dead zone) compared with several hundred micrometer-thick carbon-paste-based PSCs (Figure S3).[79] The electrode thickness is directly correlated with the device fabrication costs because both the raw material expenses and thickness must be considered collectively to determine the overall cost (Figures S4 and S5).

The FCCVD-synthesized CNT electrode-laminated metal-free all-inorganic PSCs were fabricated with a structural configuration of indium tin oxide (ITO)/SnO_2/ZnO/CPIB/CNT/P3HT. A control device with a structural configuration of ITO/SnO2/ZnO/CPIB/P3HT/Au was fabricated for comparison. The fabrication process for the metal-free all-inorganic PSCs is shown in Figure S6. The lamination of the CNT electrode is facile and direct and does not involve using chemicals. Furthermore, P3HT HTM was applied after the lamination of the CNT electrode by directly drop-casting P3HT on top of the CNT. This is unique to FCCVD-synthesized film-type CNT electrode-based PSCs and is distinct from conventional deposition methods, such as metal electrodes or paste-type carbon electrodes. The cross-sectional scanning electron microscopy (SEM) image shows that P3HT thoroughly infiltrated the CNT electrode and formed a

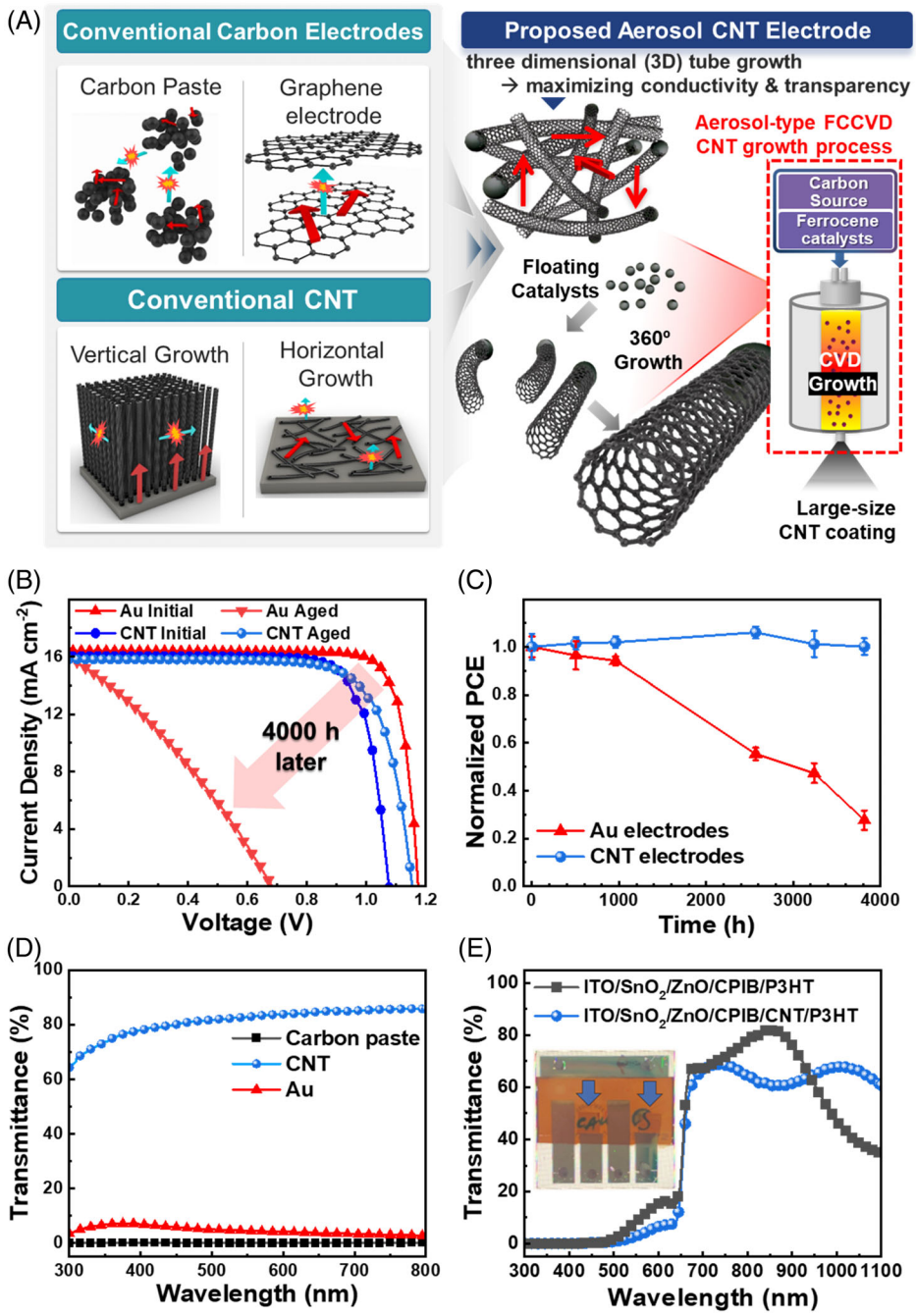

FIGURE 1 (A) Schematic illustration of the fabrication process of FCCVD-synthesized CNT. (B) *J–V* characteristics of PSCs with Au electrodes and CNT electrodes after aging for 4000 h. (C) Normalized PCE stability characteristics of unencapsulated PSCs with Au electrodes and CNT electrodes. (D) Transmission spectra of electrodes and (E) Full device structure.

Electrode	Condition	J_{SC} (mA/cm^2)	V_{OC} (V)	FF (%)	PCE (%)
Au	Initial	16.40	1.17	83.4	16.07
	Aged	15.95	0.68	31.3	3.40
CNT	Initial	16.04	1.08	79.1	13.64
	Aged	15.82	1.15	75.4	13.76

TABLE 1 Solar cell parameters of the devices for each condition in Au electrodes and CNT electrode.

moisture barrier over the perovskite active layer, providing robust protection against water and oxygen molecules (Figures S7 and S8). The CNT-based all-inorganic PSCs demonstrated a PCE of approximately 14%, which maintained more than 4000 h without encapsulation under ambient conditions (Figure 1B,C, and Table 1). In addition, open-circuit voltage (V_{OC}) of the CNT device gradually increased over aging in ambiance, which is

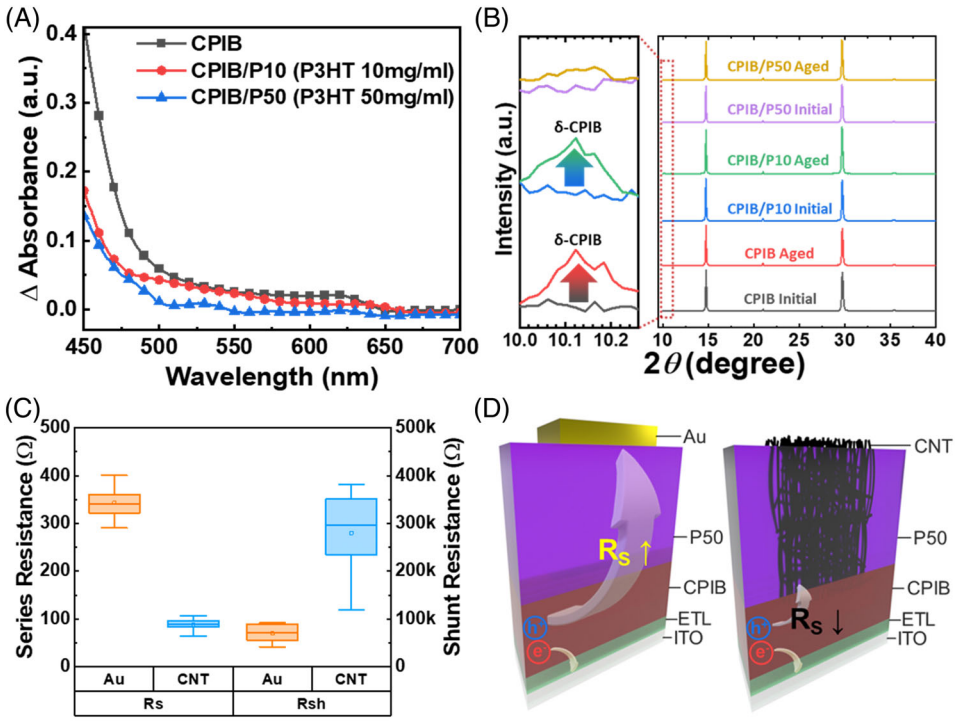

FIGURE 2 (A) Variation of the UV–vis absorption spectra and (B) XRD patterns of CPIB film with/without P10 and P50 HTM. (C) Box plot of resistance parameters of PSCs with Au electrodes and CNT electrodes. (D) Three-dimensional illustration of the difference in R_S based on the electrodes.

attributed to the π-π interactions between CNT and P3HT intensifying over time.[62,80] However, the Au metal-deposited control devices showed an initial PCE of 16.1%, which decreased rapidly over time. After 4000 h, the PCE decreased to 3.4%. This decrease is attributable to metal-ion migration-driven degradation and the inadequate moisture-blocking capability of the metal electrode. In addition to their excellent device stability, the fabricated CNT-based all-inorganic PSCs were semi-transparent, contrary to conventional metal electrode- and carbon paste-based PSCs. The FCCVD-based CNT electrodes displayed ∼82% transparency at 700 nm wavelength of the visible light, whereas the Au electrode with a thickness of ca. 40 nm showed <5% transparency. The carbon-paste electrodes were not transparent (Figure 1D). The transmittance of the entire device with a CNT top electrode was also investigated (Figure 1E). While laminating the CNT electrode decreased the transmittance of the device at 600 and 850 nm, the transmittance in the near-infrared region increased significantly. This is attributed to the optical effects of the P3HT and CNT nanohybrid films.[81,82] This implies that stacking another solar cell that absorbs near-infrared (NIR) light can boost the overall PCE by exploiting the high NIR transmittance of CNT-based PSCs, which we tested and discussed later in this manuscript.

The role of P3HT in CNT-based, metal-free, all-inorganic PSCs is crucial for achieving remarkable stability. The nanohybrid composite film of the CNT and P3HT HTM on top of the perovskite layer functioned as an effective barrier against oxygen and moisture. This implies that the device stability can be further improved by increasing the thickness of the nanocomposite film. Given that the concentration of P3HT determines the film thickness, two different concentrations of P3HT—10 mg (P10) and 50 mg (P50)—were used in the test. P10 is a widely used concentration of P3HT in conventional Au electrode-based devices. P50 is the maximum concentration that can be used, considering the solubility of P3HT in chlorobenzene. The ultraviolet–visible (UV–vis) absorption spectra of CPIB were used for stability evaluation. The CPIB film exhibited absorbance up to a wavelength of ∼660 nm, corresponding to a bandgap of ca. 1.9 eV. The film rapidly degraded when the CPIB films were left under ambient conditions for 10 d without CNT (Figures 2A and S9). The stability of the CPIB with CNT and P3HT nanocomposite films on top was studied. The CPIB with P50 on top showed much greater stability than that with P10, confirming that thicker CNT and P3HT nanocomposite films function as a better barrier. X-ray diffraction (XRD) was performed to confirm the CPIB stability from the chemical perspective (Figure 2B). The main diffraction peaks corresponding to the (100) and (200) planes of CPIB at 14.8 and 29.6°, respectively, exhibited no significant alterations for the CPIB with P50 on top. However, a noticeable shift in the CPIB peak near 10.1° was observed for the CPIB with P10, corresponding to the formation of δ-phase CPIB, which indicates degradation to CsI-PbX_2 and other impurities.[83,84] Figure S10 shows the photographic images of the CPIB films with

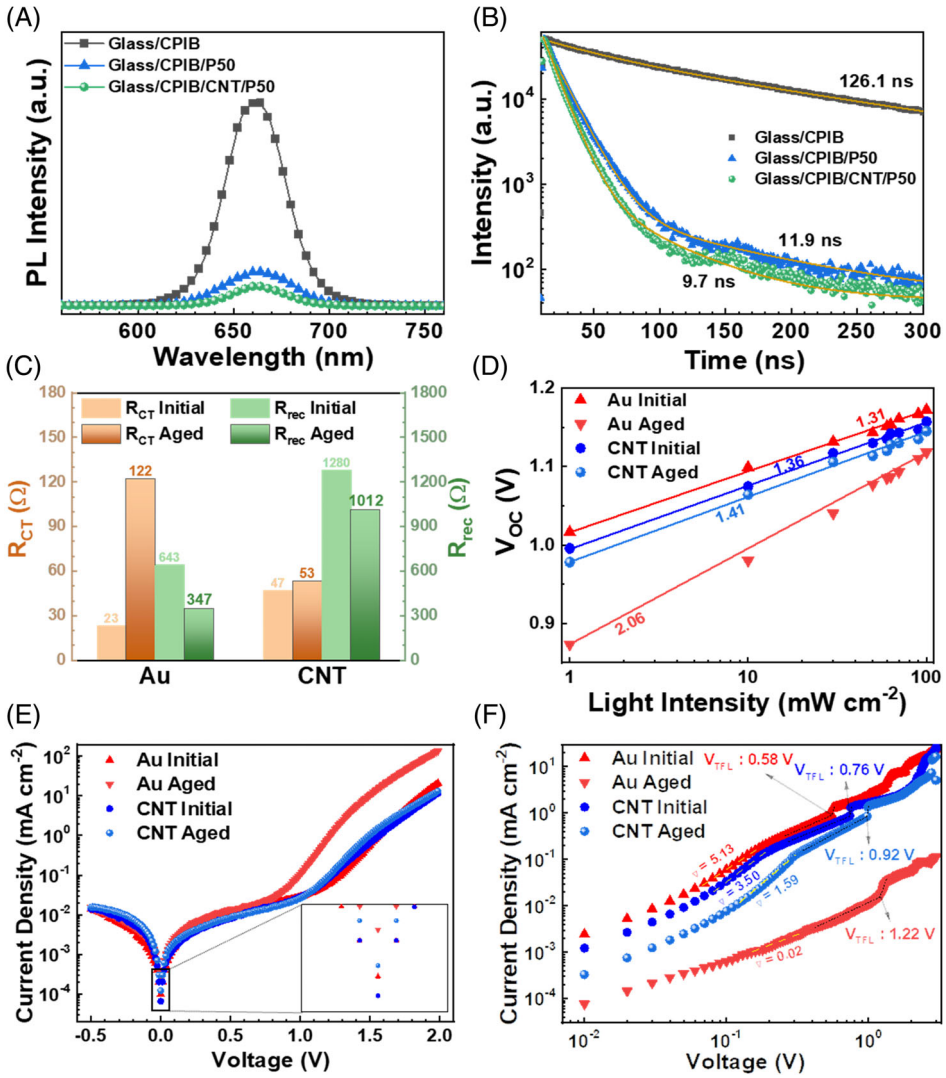

FIGURE 3 (A) PL spectra and (B) TRPL decay of the CPIB film with/without P10 and P50 HTM. (C) EQE spectra and the integrated current density of the three types of PSCs. (D) Light intensity dependent V_{OC} evaluation and (E) Dark *J*–*V* measurement and (F) SCLC measurement of different electrodes.

and without CNTs + P10 or P50, visually confirming the level of degradation. Overall, a higher P3HT concentration provides better protection against moisture penetration in the CPIB layer.

While we confirmed that the thicker nanocomposite film of CNT and P3HT was better from the device stability point of view, its effect on the photovoltaic performance had to be investigated. It is generally accepted that a thicker HTM leads to higher series resistance (R_S). This was evident in the case of Au electrode deposited devices where the P50-based device afforded R_S above 300 Ω when the P10-based device afforded R_S below 80 Ω (Figures 2C and S11). By contrast, the CNT electrode devices using P50 exhibited a much lower R_S of <100 Ω, and the devices with P10 afforded a similar low R_S of ca. 100 Ω. This phenomenon is attributed to the unique device structure of CNT-laminated solar cells, where the CNT electrode is in direct contact with the perovskite layer, ensuring efficient hole extraction regardless of the HTM concentration (Figure 2D). At the same time, a high concentration of the P3HT HTM within the CNT network effectively blocks electron recombination, as indicated by the approximately three-fold greater shunt resistance (R_{SH}) of the CNT-based devices compared with the Au electrode.

Photoluminescence (PL) and time-resolved photoluminescence (TRPL) measurements were conducted to verify the charge transport characteristics of the CNT-based devices. The CPIB exhibited a prominent PL peak at ~660 nm, indicating excellent radiative recombination, which was significantly quenched upon P3HT deposition (Figure 3A). Interestingly, the nanohybrid composite of P3HT and CNT quenched the holes more effectively. TRPL data shown in Figure 3B also confirms this trend; the biexponential lifetime of CPIB was 126.2 ns (Table S1). When P50 was applied to the CPIB to induce hole quenching, the lifetime decreased to 11.9 ns. The lifetime quenching further intensified to 9.7 ns when P50 was applied along with the CNTs, confirming the remarkable hole extraction characteristics of the CNT

+ HTM nanocomposite. Electrochemical impedance spectroscopy (EIS) was used to further investigate the charge dynamics of the CNT + HTM nanocomposite, as well as its change upon exposure to ambient conditions, in comparison to Au electrode-based conventional devices (Figures 3C and S12). Initially, the Au-based devices exhibited lower charge transport resistance (R_{CT}) and recombination resistance (R_{rec}) than the CNT-based devices, which aligns well with the Rs and R_{SH} trends found from the current density–voltage (J–V) curves. After 4000 h (aged) under ambient conditions, the Au-electrode-based devices exhibited a more than 5-fold increase in R_{CT} compared with the initial state, while the CNT-electrode-based devices showed a negligible change. The conspicuous increase in R_{CT} in the Au-based devices was owing to the traps formed by the migrated Au ions at the CPIB/P3HT interface. Similarly, R_{rec} under the V_{OC} bias conditions of the Au-based devices decreased by ~54% after 4000 h, while the CNT-based devices showed only a slight reduction of ~10%. Similarly, this significant reduction in R_{rec} in Au-based devices was due to the migration of Au ions.

We verified our hypothesis and investigated the nature of charge recombination by analyzing the light-intensity-dependent V_{OC}, which is commonly used to assess Shockley–Read–Hall (SRH) recombination. Equation (1) describes this relationship:

$$V = (nkT/q)\ln\left(J_{photo}/J_0\right) \quad (1)$$

where n is the ideality factor, k the Boltzmann constant, q the elementary charge, T the absolute temperature, J_{photo} the photocurrent, and J_0 the dark current. To extract the n and alpha values, we used a neutral density (ND) filter to vary the light intensity (Figure 3D). The value of n is typically between 1 and 2. An n value close to 1 corresponds to bimolecular charge carrier recombination, whereas a value close to 2 corresponds to SRH trap-assisted recombination.[85] The Au- and CNT-based devices showed relatively reasonable values of n (1.31 and 1.36, respectively). However, the aged Au-based devices showed a significantly increased n value of >2, indicating dominant SRH recombination, unlike the CNT-based devices, which exhibited only a slight increase in n. These results demonstrate that the FCCVD-synthesized free-standing CNT electrodes are highly effective in suppressing charge recombination arising from ion migration at the interface. In addition, the short-circuit current density (J_{SC}) was measured as a function of the incident light power density (I), as shown in Figure S13. J_{SC} follows a power-law relationship with light intensity, $J_{SC} \propto I^{\alpha}$, where $\alpha = .75$ suggests that the solar cell is influenced by space-charge limitations, whereas α approaching 1 implies minimal space-charge effects.[86,87] The initial α values for the Au-based and CNT-based devices were reasonably consistent at .825 and .830, respectively. Notably, as the Au-based devices aged, their α values showed a substantial decline, reaching nearly .75, indicating a clear prevalence of space-charge limitations. However, the CNT-based devices exhibited only a little reduction in α. These results highlight the impressive performance of the CNT electrodes in mitigating the impact of space-charge limitations during device degradation. In addition, we analyzed the dark current density–voltage (J–V) curves to compare the leakage currents occurring in the devices (Figure 3E). When a positive bias was applied to the Au electrode devices, we observed an increase in the current compared with the initial and aged states. This suggests that the increase in the leakage current was due to the degradation of the Au electrode. An increase in leakage current is associated with a decrease in shunt resistance. Furthermore, in the case of Au electrode devices, aging reduced the threshold voltage from ~1.3 to <1 V. This indicates that the excitons generated by the absorption of light in the perovskite were separated by the internal electric field, decreasing the built-in potential. By contrast, the CNT-electrode devices remained unchanged, and no significant voltage loss occurred.

Finally, we performed space-charge-limited current (SCLC) measurements on hole-only devices (ITO/NiO_x/CPIB/CNT/P3HT and ITO/NiO_x/CPIB/P3HT/Au) to compare their hole transport capabilities and existing defect concentrations. As shown in Figure 3F, the initial and aged curves of each electrode exhibit different gradients from low voltage to the ohmic, SCLC, and trap-filled limiting (TFL) regions. Using Equation (2), various constants can be simplified to enable a relative comparison of hole mobility, which serves as a measure of the charge-transport capability. Similarly, using Equation (3), the defect concentration can be determined.

$$J = 9/8 \times \varepsilon_0 \varepsilon_r \mu \left(V^2/L^3\right) \rightarrow \mu \propto k\left(\mathrm{J/V^2}\right) \quad (2)$$

$$n_{trap} = 2\varepsilon_r V_{TFL}/qL^2 \rightarrow n_{trap} \propto kV_{TFL} \quad (3)$$

The initial hole mobility of the Au electrode was ~1.5 times superior to that of the CNT electrode, demonstrating the clear advantage of the expensive metal electrode arising from the superior electrical conductivity of Au. However, in the aged stage, the reverse phenomenon was observed. The CNT electrode exhibited a remarkable 80-fold increase in hole mobility compared to the Au electrode, indicating that the migration of Au ions and

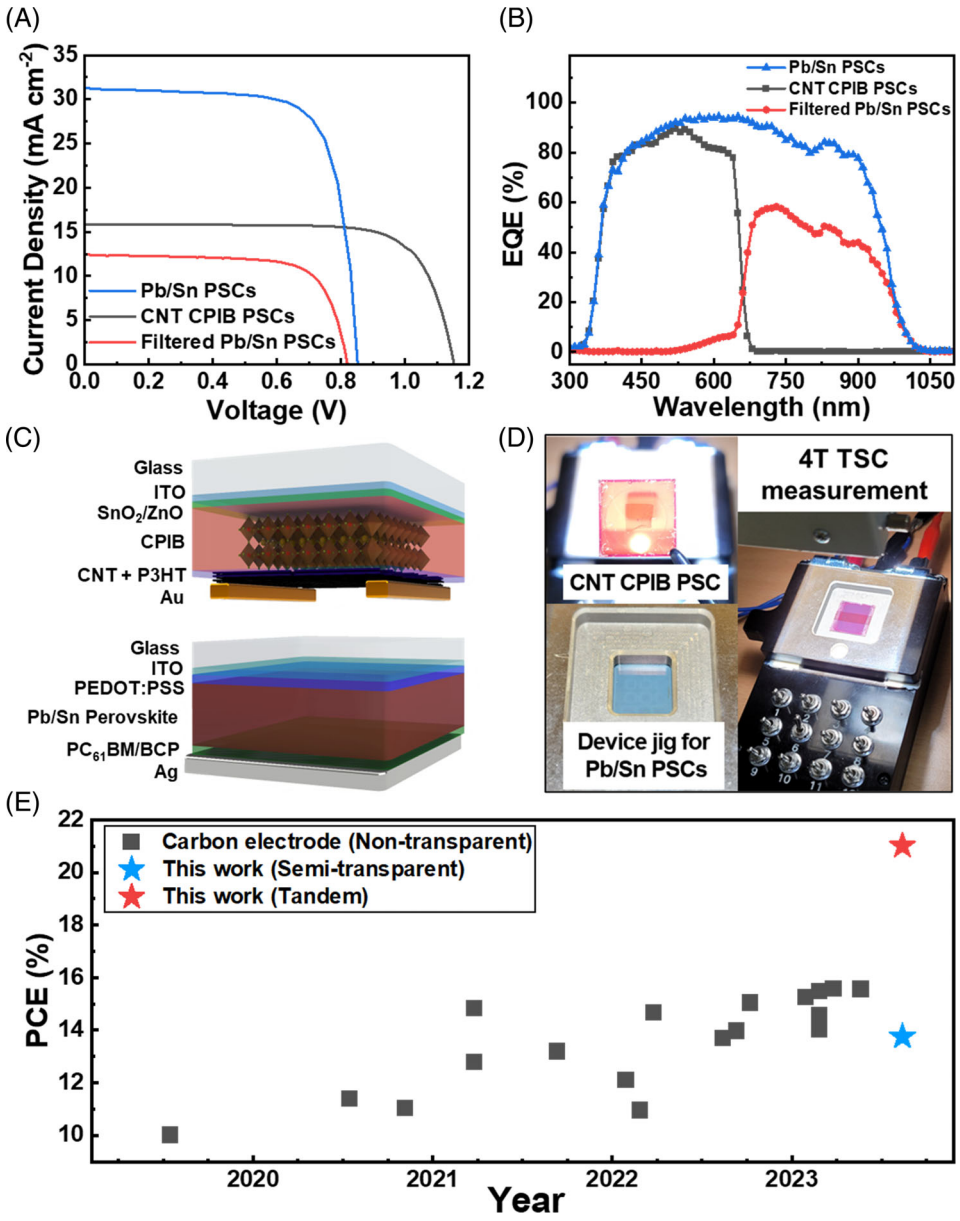

FIGURE 4 (A) *J–V* curves and (B) EQE spectra of the PSCs. (C) Schematic illustration of the 4T-PSCs. (D) Photographic images of the single PSCs (left) and operation 4T-PSCs (right). (E) Plot of PCE as a function of year for comparison other carbon-based PSCs.

degradation of perovskites by moisture in air significantly lowered the hole mobility of the entire device and the conductivity of Au. From the defect concentration revealed by the V_{TFL} values, the Au-based devices show lower V_{TFL} values than the CNT-based devices, revealing that not the passivation effect of CNTs but no metal-ion migration and the moisture barrier capability are responsible for the excellent stability and performance of the FCCVD-synthesized CNT electrode-based metal-free PSCs. Expectedly, the V_{TFL} of the Au-based device increased by ~110% after aging, while the CNT-based device showed only a ~20% increase. This confirms the remarkable stability of FCCVD-synthesized CNT electrode-based devices.

Conventional carbon-based PSCs have limited applications in tandem configurations owing to the opacity of carbon paste. However, the semi-transparent CNT CPIB PSCs demonstrated high transmittance in the NIR region (Figure 1E), making them suitable for integration into 4T perovskite–perovskite TSCs. The narrow-bandgap PSC showed a PCE of 19.7%, whereas the semitransparent CNT-based CPIB PSCs, used as filters in the 4T tandem configuration, achieved a PCE of 7.4%. Consequently, the overall PCE of the 4T TSCs reached an impressive value of 21.1% (Figure 4A, Table 2). In addition, the external quantum efficiency (EQE) spectra shown in Figure 4B indicate that the narrow-bandgap PSCs successfully absorbed the light transmitted through the top CNT CPIB PSCs. Figure 4C illustrates a schematic representation of the TSCs, while Figure 4D provides a photographic image of the experimental setup for tandem measurements. The obtained a PCE of 13.8% for the top all-inorganic PSC using FCCVD-synthesized CNTs, which was the highest

TABLE 2 Solar cell parameters of the component cells and the four-terminal perovskite/perovskite tandem solar cells efficiency.

Sample	J_{SC} (mA/cm^2)	V_{OC} (V)	FF (%)	PCE (%)
Low-E_g Pb/Sn PSCs	31.26	0.85	73.9	19.70
CNT based CPIB PSCs	15.82	1.15	75.4	13.76
Filtered Pb/Sn PSCs	12.43	0.82	72.1	7.35
4T TSCs				21.11

among the carbon electrode-based semi-transparent all-inorganic PSCs. Furthermore, the PCE of 21.1% exhibited by the 4T TSCs configuration demonstrates the potential that no other carbon top electrode-based PSCs could achieve within the scope of all-inorganic PSCs (Figure 4E, Table S2). The CNT-based CPIB PSCs developed in this study not only exhibit remarkable potential for long-term stability but also offer enhanced transparency compared to Au electrodes, enabling the possibility of semi-transparent BIPV applications. Furthermore, their compatibility with tandem solar cell configurations further strengthens their significance in PSCs.

3 | CONCLUSION

This study presents the first application of FCCVD-synthesized CNT electrodes in all-inorganic PSCs. Combining CNT and all-inorganic perovskite technologies, which boost the device stability of perovskite systems, achieved a remarkable device stability of more than 4000 h in air without encapsulation. By contrast, conventional metal electrode devices deteriorate within 1000 h, even if they are inorganic. This enhanced stability is attributed to the robust nanohybrid film formed by CNT and HTM. This film not only serves as an effective protective layer but also acts as a charge collector and electrode, circumventing the need for traditional costly metal top electrodes. Furthermore, the recorded PCE of 13.8% for the CNT-based devices was the highest among the semi-transparent metal-free all-inorganic PSCs. The obtained value is high considering that all-inorganic PSCs intrinsically exhibit much lower efficiency than their organic–inorganic hybrid counterparts at the expense of greater thermal and air stability. In addition, owing to their semi-transparent nature, the CNT-based devices show a critical advantage for BIPV and tandem applications, evidenced by the impressive 21.1% PCE of our tested four-terminal tandem devices. This innovative study emphasizes the potential of all-inorganic PSCs with CNT electrodes in setting new standards for stability, transparency, and efficiency. Our findings pave the way for a transformative strategy to advancing perovskite solar cells toward real-world applications, showing a promise for renewable energy.

4 | EXPERIMENTAL SECTION

4.1 | Materials

ITO substrates were purchased from AMGlass. Dimethylformamide (DMF 99.5%), 2-methoxyethanol (2-ME, 99%), dimethyl sulfoxide (DMSO, 99.8%), and ethanolamine (99%) were purchased from Samchun Chemicals. Diiodomethane (99%), tin oxide (SnO_2) colloidal solution (15% in H_2O), cesium iodide (CsI, 99.99%), and tin(II) iodide (SnI_2, 99.999%) were purchased from Alfa Aesar. In addition, nickel(II) nitrate hexahydrate ($Ni(NO_3)_2{\cdot}6H_2O$, 99.999%), tin(II) fluoride (SnF_2, 99%), lead bromide ($PbBr_2$, 99.99%), and zinc acetate dihydrate ($Zn(CH_3CO)_2{\cdot}2H_2O$, 99.99%) were obtained from Sigma Aldrich. Lead iodide (PbI_2, 99.99%) and phenethylammonium iodide (PEAI, >98.0%) were purchased from Tokyo Chemical Industry (TCI chemicals). Chlorobenzene (CB 99%, GR grade) was purchased from Wako Chemicals. The formamidinium iodide (FAI) was purchased from GreatCell Solar. $PC_{61}BM$ and BCP were purchased from OSM. Poly(3-hexylthiophene-2,-5-diyl) (P3HT) was purchased from RIEKE Metals. Poly(3,-4-ethylenedioxythiophene) polystyrene sulfonate (PEDOT:PSS, PVP AI 4083) was purchased from Clevios.

4.2 | FCCVD-based CNT synthesis

The CNTs were synthesized using an aerosol FCCVD method involving ferrocene vapor decomposition under a CO atmosphere. First, the catalyst precursor was vaporized by passing CO (under ambient temperature) through a cartridge filled with ferrocene powder at ambient temperature. The generated ferrocene vapor was introduced into the high-temperature zone of the ceramic tube reactor using a water-cooled probe and mixed with additional CO. To establish a stable growth of CNTs, a controlled amount of CO_2 was mixed with the CO carbon source. Finally, the CNTs were directly collected downstream of the reactor by filtering the flow through a nitrocellulose membrane filter (Millipore Corp., USA; HAWP, 0.45 μm pore diameter). The collection time determined both the transparency and conductivity of the CNT films.

4.3 | CPIB PSC fabrication

The ITO-coated glass substrates were successively cleaned with acetone and IPA for 20 min in each solution using an ultrasonic bath and were dried in an oven at 95°C for 30 min. Subsequently, the substrates were cooled to room temperature and subjected to ultraviolet-ozone (UV-O_3) treatment to increase the surface energy and remove organic contaminants, if any, on the substrate surface. Next, a SnO_2 precursor solution (1.5% in H_2O) was deposited on top of the UV-O_3 treated substrates at a continuous spinning speed of 1000 and 3000 rpm for 0.5 and 30 s, respectively. The SnO_2-coated ITO substrates were annealed at 150°C for 30 min. For the zinc oxide (ZnO) precursor solution, 2 mL of 2-ME and 61.7 μL of ethanolamine were added to 0.2195 g of dehydrated zinc acetate and stirred at 60°C for 2 h. The bilayer of the ZnO electron transport material was spin-coated on SnO_2/ITO substrates with successive spinning speeds of 1000 and 5000 rpm for 0.5 and 30 s, respectively. The ZnO-deposited SnO_2/ITO substrates were heated at 170°C for 30 min. 1.2 M CPIB perovskite solution, 0.3118 g of CsI, 0.2766 g of PbI_2, 0.8 mg of PEAI, and 0.2202 g $PbBr_2$ were dissolved in a mixture of DMSO and DMF (7:3 v/v). The prepared solution was stirred for 12 h in a nitrogen (N_2) filled glovebox at room temperature. Then, the prepared CPIB perovskite solutions were coated on the ZnO/SnO_2/ITO substrates at 3000 rpm for 40 s. Dynamic hot air (230°C) using a hot air gun (Bosch, GHG 630 DCE hot air gun – 0601 94C 740) was blown on top of substrates for 8 to 22 s during spin coating to promote perovskite nucleation. The hot air-treated substrates were sintered at 240°C for 10 min to complete the crystallization process. After cooling the samples, CNTs were laminated onto the crystallized perovskite layer. Subsequently, solutions of P3HT (10 and 50 mg mL^{-1} in CB) were spin-coated onto the samples at 3000 rpm for 30 s and annealed at 100°C for 5 min. For hole-only devices, the NiO_x as bottom HTM was deposited at 5000 rpm for 50 s and annealed at 300°C for 60 min. For reference samples, a 120 nm Au layer was deposited as a metal electrode using a thermal evaporator (<1 × 10^{-6} Torr) to complete the cell structure (Au/P3HT/perovskite/ZnO/SnO_2/ITO). The active cell area was 8.03 mm^2, defined using a shadow mask.

4.4 | Narrow E_g Pb/Sn PSCs fabrication

To prepare the narrow band gap perovskite precursor solution with a composition of 1.2 M $FA_{0.83}Cs_{0.17}Sn_{0.5}Pb_{0.5}I_3$, we dissolved FAI (0.83 m), CsI (0.17 m), PbI_2 (0.5 m), and SnI_2 (0.5 m) in a mixed solvent of DMF:DMSO (4:1) along with an additive of SnF_2 (0.05 m). The ITO substrates were coated with PEDOT:PSS by spin coating at 5000 rpm for 50 s under ambient conditions. The PEDOT:PSS-coated ITO substrates were subsequently annealed at 150°C for 20 min on a hotplate to serve as HTM. Subsequently, the PEDOT:PSS-coated ITO substrates were transferred to a N_2-filled glove box to deposit the narrow-band-gap perovskite layer. The perovskite precursor solution was spin-coated onto the substrate at 5000 rpm for 30 s. During the spin coating process, 0.3 mL of a $PC_{61}BM$ solution dissolved in toluene (1 mg mL^{-1}) was added dropwise to the sample. The perovskite-coated substrates were annealed first at 65°C for 1 min and then at 100°C for 30 min. As for the electron-transporting layer (ETL), a solution of $PC_{61}BM$ (20 mg mL^{-1} in CB) was spin-coated onto the perovskite film at 1500 rpm for 35 s and subsequently annealed at 80°C for 10 min. For the final step, a solution of BCP (0.5 mg mL^{-1} in IPA) was spin-coated at 4000 rpm for 20 s without any post-annealing. The top electrode, made of Ag, was deposited using thermal evaporation under high vacuum conditions (<1 × 10^{-6} Torr) with a shadow mask. Each solar-cell device was 4 mm^2.

4.5 | Device characterization

J–V curves of the PSCs under light were constructed using a source meter (Keithley 2400, Tektronix) at a step voltage of 20 mV and delay time of 50 ms in both the forward and reverse scan directions. A metal aperture mask with an area of 0.0780 cm^2 was used during *J–V* measurements. AM 1.5G illumination was simulated using a solar simulator (Solar 3A Class, Oriel) with a KG-5-filtered silicon standard cell. *J–V* curves were obtained under dark conditions using a probe station built inside a dark-shield box. Cross-sectional SEM measurements were conducted using field-emission SEM (Carl Zeiss). The external quantum efficiency (EQE) spectra were characterized using a monochromator (MonoRa500i, DongWoo Optron) and a CompactStat instrument (Ivium Technologies). Electrochemical impedance spectroscopy (EIS) measurements for the Nyquist plots were also conducted on CompactStat equipment under various bias and dark conditions in the frequency range of 2 MHz to 10 Hz. Perovskite phase degradation was analyzed using XRD (D8-Advance, Bruker). Transmittance and absorbance (Tauc plot) spectra were acquired using a UV–Vis spectrometer (UV-2700, Shimadzu).

AUTHOR CONTRIBUTIONS

Saemon Yoon: Writing – original draft, investigation, formal Analysis. **Il Hyun Lee:** Writing – original draft, investigation, visualization. **Jiye Han:** Visualization.

Jitendra Bahadur: Investigation. **Seojun Lee:** Investigation. **Sangsu Lee:** Investigation. **Dong Suk Kim:** Investigation, writing – review & editing. **B. Mikladal:** Synthesis of Carbon Nanotubes. **Esko I. Kauppinen:** Synthesis of Carbon Nanotubes. **Dong-Won Kang:** Resources, supervision, writing – review & editing. **Il Jeon:** Resources, supervision, writing – review & editing, All authors have given approval to the final version of the manuscript.

ACKNOWLEDGMENTS

S. Y. and I. L. contributed equally to this study. This work was supported by the National Research Foundation of Korea funded by the Ministry of Science and ICT (MSIT) of Korea (NRF-2023R1A2C3007358, RS-2023K2A9A2A23000283, RS-2023-00217270, RS-2023-00212744). Glove boxes from MBraun Co. Ltd. provided by the SAINT-MBraun Application Laboratory were used in this study.

CONFLICT OF INTEREST STATEMENT

The authors declare no conflict of interest.

ORCID

Il Jeon https://orcid.org/0000-0002-4220-8374

REFERENCES

1. Schoonman J. Organic–inorganic lead halide perovskite solar cell materials: a possible stability problem. *Chem Phys Lett*. 2015;619(5):193-195. doi:10.1016/j.cplett.2014.11.063
2. Lin C. Stabilizing organic–inorganic lead halide perovskite solar cells with efficiency beyond 20%. *Front Chem*. 2020;8:592. doi:10.3389/fchem.2020.00592
3. Mitzi DB, Yuan M, Liu W, et al. A high-efficiency solution-deposited thin-film photovoltaic device. *Adv Mater*. 2008; 20(19):3657-3662. doi:10.1002/adma.200800555
4. Gao L, Zhang ZG, Xue L, et al. All-polymer solar cells based on absorption-complementary polymer donor and acceptor with high power conversion efficiency of 8.27%. *Adv Mater*. 2016; 28(9):1884-1890. doi:10.1002/adma.201504629
5. Chen Y-H, Lin L-Y, Lu C-W, et al. Vacuum-deposited small-molecule organic solar cells with high power conversion efficiencies by judicious molecular design and device optimization. *J Am Chem Soc*. 2012;134(33):13616-13623. doi:10.1021/ja301872s
6. Song Z, McElvany CL, Phillips AB, et al. A technoeconomic analysis of perovskite solar module manufacturing with low-cost materials and techniques. *Energ Environ Sci*. 2017;10(6): 1297-1305. doi:10.1039/C7EE00757D
7. Dutta NS, Noel NK, Arnold CB. Crystalline nature of colloids in methylammonium lead halide perovskite precursor inks revealed by cryo-electron microscopy. *J Phys Chem Lett*. 2020; 11(15):5980-5986. doi:10.1021/acs.jpclett.0c01975
8. Xu X, Wang W, Zhou W, Shao Z. Recent advances in novel nanostructuring methods of perovskite electrocatalysts for energy-related applications. *Small Methods*. 2018;2(7):1800071. doi:10.1002/smtd.201800071
9. Correa-Baena J-P, Saliba M, Buonassisi T, et al. Promises and challenges of perovskite solar cells. *Science*. 2017;358(6364): 739-744. doi:10.1126/science.aam6323
10. Chang NL, Yi Ho-Baillie AW, Basore PA, Young TL, Evans R, Egan RJ. A manufacturing cost estimation method with uncertainty analysis and its application to perovskite on glass photovoltaic modules. *Prog Photovolt Res Appl*. 2017;25(5):390-405. doi:10.1002/pip.2871
11. Berhe TA, Su W-N, Chen C-H, et al. Organometal halide perovskite solar cells: degradation and stability. *Energ Environ Sci*. 2016;9(2):323-356. doi:10.1039/C5EE02733K
12. Jain P, Ramachandran V, Clark RJ, et al. Multiferroic behavior associated with an order−disorder hydrogen bonding transition in metal−organic frameworks (MOFs) with the perovskite ABX3 architecture. *J Am Chem Soc*. 2009;131(38):13625-13627. doi:10.1021/ja904156s
13. Gladkikh V, Kim DY, Hajibabaei A, Jana A, Myung CW, Kim KS. Machine learning for predicting the band gaps of ABX3 perovskites from elemental properties. *J Phys Chem C*. 2020;124(16):8905-8918. doi:10.1021/acs.jpcc.9b11768
14. Lyu M, Yun J-H, Cai M, et al. Organic–inorganic bismuth (III)-based material: a lead-free, air-stable and solution-processable light-absorber beyond organolead perovskites. *Nano Res*. 2016; 9(3):692-702. doi:10.1007/s12274-015-0948-y
15. Brennan MC, Draguta S, Kamat PV, Kuno M. Light-induced anion phase segregation in mixed halide perovskites. *ACS Energy Lett*. 2017;3(1):204-213. doi:10.1021/acsenergylett.7b01151
16. Kim M, Motti SG, Sorrentino R, Petrozza A. Enhanced solar cell stability by hygroscopic polymer passivation of metal halide perovskite thin film. *Energ Environ Sci*. 2018;11(9):2609-2619. doi:10.1039/C8EE01101J
17. Kwon H, Lim JW, Han J, et al. Towards efficient and stable perovskite solar cells employing non-hygroscopic F4-TCNQ doped TFB as the hole-transporting material. *Nanoscale*. 2019; 11(41):19586-19594. doi:10.1039/C9NR05719F
18. Kulbak M, Cahen D, Hodes G. How important is the organic part of lead halide perovskite photovoltaic cells? Efficient CsPbBr3 cells. *J Phys Chem Lett*. 2015;6(13):2452-2456. doi:10.1021/acs.jpclett.5b00968
19. Li C, Tscheuschner S, Paulus F, et al. Iodine migration and its effect on hysteresis in perovskite solar cells. *Adv Mater*. 2016; 28(12):2446-2454. doi:10.1002/adma.201503832
20. Courtier NE, Cave JM, Foster JM, Walker AB, Richardson G. How transport layer properties affect perovskite solar cell performance: insights from a coupled charge transport/ion migration model. *Energ Environ Sci*. 2019;12(1):396-409. doi:10.1039/C8EE01576G
21. Warren WL, Vanheusden K, Dimos D, Pike GE, Tuttle BA. Oxygen vacancy motion in perovskite oxides. *J Am Ceram Soc*. 1996;79(2):536-538. doi:10.1111/j.1151-2916.1996.tb08162.x
22. Kawai H, Kuwano J. Lithium ion conductivity of A-site deficient perovskite solid solution La0.67 − x Li3x TiO_3. *J Electrochem Soc*. 1994;141(7):L78-L79. doi:10.1149/1.2055043
23. Giuliano G, Cataldo S, Scopelliti M, et al. Nonprecious copper-based transparent top electrode via seed layer–assisted thermal evaporation for high-performance semitransparent n-i-p perovskite solar cells. *Adv Mater Technol*. 2019;4(5):1800688. doi:10.1002/admt.201800688

24. Li Z, Klein TR, Kim DH, et al. Scalable fabrication of perovskite solar cells. *Nat Rev Mater*. 2018;3(4):1-20. doi:10.1038/natrevmats.2018.17
25. Zhou Y, Yin Y, Zuo X, et al. Enhancing chemical stability and suppressing ion migration in $CH_3NH_3PbI_3$ perovskite solar cells via direct backbone attachment of polyesters on grain boundaries. *Chem Mater*. 2020;32(12):5104-5117. doi:10.1021/acs.chemmater.0c00995
26. Wei D, Wang T, Ji J, et al. Photo-induced degradation of lead halide perovskite solar cells caused by the hole transport layer/metal electrode interface. *J Mater Chem A*. 2016;4(5):1991-1998. doi:10.1039/C5TA08622A
27. Ju M-G, Chen M, Zhou Y, et al. Toward eco-friendly and stable perovskite materials for photovoltaics. *Joule*. 2018;2(7):1231-1241. doi:10.1016/j.joule.2018.04.026
28. Giuliano G, Bonasera A, Arrabito G, Pignataro B. Semitransparent perovskite solar cells for building integration and tandem photovoltaics: design strategies and challenges. *Solar RRL*. 2021;5(12):2100702. doi:10.1002/solr.202100702
29. Wang Y, Dar MI, Ono LK, et al. Thermodynamically stabilized β-$CsPbI_3$–based perovskite solar cells with efficiencies >18%. *Science*. 2019;365(6453):591-595. doi:10.1126/science.aav8680
30. Lau CFJ, Wang Z, Sakai N, et al. Fabrication of efficient and stable $CsPbI_3$ perovskite solar cells through cation exchange process. *Adv Energy Mater*. 2019;9(36):1901685. doi:10.1002/aenm.201901685
31. Liu C, Yang Y, Xia X, et al. Soft template-controlled growth of high-quality $CsPbI_3$ films for efficient and stable solar cells. *Adv Energy Mater*. 2020;10(9):1903751. doi:10.1002/aenm.201903751
32. Chen W, Zhang J, Xu G, et al. A semitransparent inorganic perovskite film for overcoming ultraviolet light instability of organic solar cells and achieving 14.03% efficiency. *Adv Mater*. 2018;30(21):1800855. doi:10.1002/adma.201800855
33. Han Q, Yang S, Wang L, et al. The sulfur-rich small molecule boosts the efficiency of carbon-based $CsPbI_2Br$ perovskite solar cells to approaching 14%. *Solar Energy*. 2021;216(1):351-357. doi:10.1016/j.solener.2021.01.030
34. Bahadur J, Ryu J, Lee D-G, et al. In-situ surface defects passivation with small carbon chain molecules for highly efficient, air-processed inorganic $CsPbI_2Br$ perovskite photovoltaics. *Appl Surf Sci*. 2023;614:156229. doi:10.1016/j.apsusc.2022.156229
35. Yu L, Guo T, Yuan H, et al. Effective lewis base additive with S-donor for efficient and stable $CsPbI_2Br$ based perovskite solar cells. *Chem Eng J*. 2021;420:129931. doi:10.1016/j.cej.2021.129931
36. Bahadur J, Cho S, Pandey P, et al. Surface defect passivation of all-inorganic $CsPbI_2Br$ perovskites via fluorinated ionic liquid for efficient outdoor/indoor photovoltaics processed in ambient air. *Appl Surf Sci*. 2023;637:157901. doi:10.1016/j.apsusc.2023.157901
37. Bahadur J, Ryu J, Pandey P, Cho S, Cho JS, Kang D-W. In situ-crystal reconstruction strategy-based highly efficient air-processed inorganic $CsPbI_2Br$ perovskite photovoltaics for indoor, outdoor, and switching applications. *Nanoscale*. 2023;15(8):3850-3863. doi:10.1039/D2NR06230E
38. Zhang J, Wang Z, Mishra A, et al. Intermediate phase enhances inorganic perovskite and metal oxide interface for efficient photovoltaics. *Joule*. 2020;4(1):222-234. doi:10.1016/j.joule.2019.11.007
39. Xiao H, Zuo C, Yan K, et al. Highly efficient and air-stable inorganic perovskite solar cells enabled by polyactic acid modification. *Adv Energy Mater*. 2023;13(32):2300738. doi:10.1002/aenm.202300738
40. Dong C, Han X, Zhao Y, Li J, Chang L, Zhao W. A green anti-solvent process for high performance carbon-based $CsPbI_2Br$ all-inorganic perovskite solar cell. *Solar RRL*. 2018;2(9):1800139. doi:10.1002/solr.201800139
41. Chen W, Chen H, Xu G, et al. Precise control of crystal growth for highly efficient $CsPbI_2Br$ perovskite solar cells. *Joule*. 2019;3(1):191-204. doi:10.1016/j.joule.2018.10.011
42. Dong C, Han X, Li W, Qiu Q, Wang J. Anti-solvent assisted multi-step deposition for efficient and stable carbon-based $CsPbI_2Br$ all-inorganic perovskite solar cell. *Nano Energy*. 2019;59:553-559. doi:10.1016/j.nanoen.2019.02.075
43. Duan C, Cui J, Zhang M, et al. Precursor engineering for ambient-compatible antisolvent-free fabrication of high-efficiency $CsPbI_2Br$ perovskite solar cells. *Adv Energy Mater*. 2020;10(22):2000691. doi:10.1002/aenm.202000691
44. Si H, Liao Q, Zhang Z, et al. An innovative design of perovskite solar cells with Al_2O_3 inserting at ZnO/perovskite interface for improving the performance and stability. *Nano Energy*. 2016;22:223-231. doi:10.1016/j.nanoen.2016.02.025
45. Hou F, Su Z, Jin F, et al. Efficient and stable planar heterojunction perovskite solar cells with an MoO_3/PEDOT:PSS hole transporting layer. *Nanoscale*. 2015;7(21):9427-9432. doi:10.1039/C5NR01864A
46. Zou M, Xia X, Jiang Y, et al. Strengthened perovskite/fullerene interface enhances efficiency and stability of inverted planar perovskite solar cells via a tetrafluoroterephthalic acid interlayer. *ACS Appl Mater Interfaces*. 2019;11(36):33515-33524. doi:10.1021/acsami.9b12961
47. Li Z, Liu C, Zhang X, Ren G, Han W, Guo W. Developing 1D Sb-embedded carbon nanorods to improve efficiency and stability of inverted planar perovskite solar cells. *Small*. 2019;15(1):1804692. doi:10.1002/smll.201804692
48. Bai Y, Dong Q, Shao Y, et al. Enhancing stability and efficiency of perovskite solar cells with crosslinkable silane-functionalized and doped fullerene. *Nat Commun*. 2016;7(1):12806. doi:10.1038/ncomms12806
49. Zhang X, Gao N, Li Y, et al. A solution-processed dopant-free tin phthalocyanine (SnPc) hole transport layer for efficient and stable carbon-based $CsPbI_2Br$ planar perovskite solar cells prepared by a low-temperature process. *ACS Appl Energy Mater*. 2020;3(8):7832-7843. doi:10.1021/acsaem.0c01184
50. Zhang F, Zhu K. Additive engineering for efficient and stable perovskite solar cells. *Adv Energy Mater*. 2020;10(13):1902579. doi:10.1002/aenm.201902579
51. Ullah S, Wang J, Yang P, et al. All-inorganic $CsPbI_2Br$ perovskite solar cells: recent developments and challenges. *Energ Technol*. 2021;9(12):2100691. doi:10.1002/ente.202100691
52. Gao F, Zhao Y, Zhang X, You J. Recent progresses on defect passivation toward efficient perovskite solar cells. *Adv Energy Mater*. 2020;10(13):1902650. doi:10.1002/aenm.201902650
53. Zhang Y, Ng S-W, Lu X, Zheng Z. Solution-processed transparent electrodes for emerging thin-film solar cells. *Chem Rev*. 2020;120(4):2049-2122. doi:10.1021/acs.chemrev.9b00483

54. Wieland L, Li H, Rust C, Chen J, Flavel BS. Carbon nanotubes for photovoltaics: from lab to industry. *Adv Energy Mater*. 2021; 11(3):2002880. doi:10.1002/aenm.202002880
55. He R, Huang X, Chee M, Hao F, Dong P. Carbon-based perovskite solar cells: from single-junction to modules. *Carbon Energy*. 2019;1(1):109-123. doi:10.1002/cey2.11
56. Zhang Q, Nam JS, Han J, et al. Large-diameter carbon nanotube transparent conductor overcoming performance–yield tradeoff. *Adv Funct Mater*. 2022;32(11):2103397. doi:10.1002/adfm.202103397
57. Yoon J, Kim U, Yoo Y, et al. Foldable perovskite solar cells using carbon nanotube-embedded ultrathin polyimide conductor. *Adv Sci*. 2021;8(7):2004092. doi:10.1002/advs.202004092
58. Nasibulin AG, Kaskela A, Mustonen K, et al. Multifunctional free-standing single-walled carbon nanotube films. *ACS Nano*. 2011;5(4):3214-3221. doi:10.1021/nn200338r
59. Jeon I, Cui K, Chiba T, et al. Direct and dry deposited single-walled carbon nanotube films doped with MoOxas electron-blocking transparent electrodes for flexible organic solar cells. *J Am Chem Soc*. 2015;137(25):7982-7985. doi:10.1021/jacs.5b03739
60. Jeon I, Chiba T, Delacou C, et al. Single-walled carbon nanotube film as electrode in indium-free planar heterojunction perovskite solar cells: investigation of electron-blocking layers and dopants. *Nano Lett*. 2015;15(10):6665-6671. doi:10.1021/acs.nanolett.5b02490
61. Mei A, Li X, Liu L, et al. A hole-conductor–free, fully printable mesoscopic perovskite solar cell with high stability. *Science*. 2014;345(6194):295-298. doi:10.1126/science.1254763
62. Zhang G, Zhang J, Pan Z, Rao H, Zhong X. Enhancing hole extraction via carbon nanotubes/poly(3-hexylthiophene) composite for carbon-based $CsPbI_2Br$ solar cells with a new record efficiency. *Sci China Mater*. 2023;66:1727-1735. doi:10.1007/s40843-022-2343-7
63. Chu Q-Q, Ding B, Peng J, et al. Highly stable carbon-based perovskite solar cell with a record efficiency of over 18% via hole transport engineering. *J Mater Sci Technol*. 2019;35(6):987-993. doi:10.1016/j.jmst.2018.12.025
64. Jeon I, Xiang R, Shawky A, Matsuo Y, Maruyama S. Single-walled carbon nanotubes in emerging solar cells: synthesis and electrode applications. *Adv Energy Mater*. 2019;9(23):1801312. doi:10.1002/aenm.201801312
65. Seo S, Akino K, Nam JS, et al. Multi-functional MoO_3 doping of carbon-nanotube top electrodes for highly transparent and efficient semi-transparent perovskite solar cells. *Adv Mater Interfaces*. 2022;9(11):2101595. doi:10.1002/admi.202101595
66. Li Z, Kulkarni SA, Boix PP, et al. Laminated carbon nanotube networks for metal electrode-free efficient perovskite solar cells. *ACS Nano*. 2014;8(7):6797-6804. doi:10.1021/nn501096h
67. Lee J-W, Jeon I, Lin H-S, et al. Vapor-assisted ex-situ doping of carbon nanotube toward efficient and stable perovskite solar cells. *Nano Lett*. 2018;19(4):2223-2230. doi:10.1021/acs.nanolett.8b04190
68. Jeon I, Shawky A, Seo S, et al. Carbon nanotubes to outperform metal electrodes in perovskite solar cellsviadopant engineering and hole-selectivity enhancement. *J Mater Chem A*. 2020;8(22): 11141-11147. doi:10.1039/D0TA03692G
69. Jeon I, Shawky A, Lin H-S, et al. Controlled redox of lithium-ion endohedral fullerene for efficient and stable metal electrode-free perovskite solar cells. *J Am Chem Soc*. 2019; 141(42):16553-16558. doi:10.1021/jacs.9b06418
70. Aitola K, Sveinbjörnsson K, Correa-Baena J-P, et al. Carbon nanotube-based hybrid hole-transporting material and selective contact for high efficiency perovskite solar cells. *Energ Environ Sci*. 2016;9(2):461-466. doi:10.1039/C5EE03394B
71. Aitola K, Domanski K, Correa-Baena JP, et al. High temperature-stable perovskite solar cell based on low-cost carbon nanotube hole contact. *Adv Mater*. 2017;29(17):1606398. doi:10.1002/adma.201606398
72. Wang Z, Zhu X, Zuo S, et al. 27%-efficiency four-terminal perovskite/silicon tandem solar cells by sandwiched gold nanomesh. *Adv Funct Mater*. 2020;30(4):1908298. doi:10.1002/adfm.201908298
73. Lamanna E, Matteocci F, Calabrò E, et al. Mechanically stacked, two-terminal graphene-based perovskite/silicon tandem solar cell with efficiency over 26%. *Joule*. 2020;4(4):865-881. doi:10.1016/j.joule.2020.01.015
74. Kim JY, Lee K, Coates NE, et al. Efficient tandem polymer solar cells fabricated by all-solution processing. *Science*. 2007; 317(5835):222-225. doi:10.1126/science.1141711
75. Choi JM, Han J, Yoon J, Kim S, Jeon I, Maruyama S. Overview and outlook on graphene and carbon nanotubes in perovskite photovoltaics from single-junction to tandem applications. *Adv Funct Mater*. 2022;32(42):2204594. doi:10.1002/adfm.202204594
76. Chen B, Bai Y, Yu Z, et al. Efficient semitransparent perovskite solar cells for 23.0%-efficiency perovskite/silicon four-terminal tandem cells. *Adv Energy Mater*. 2016;6(19):1601128. doi:10.1002/aenm.201601128
77. Ameri T, Li N, Brabec CJ. Highly efficient organic tandem solar cells: a follow up review. *Energ Environ Sci*. 2013;6(8):2390-2413. doi:10.1039/c3ee40388b
78. Ahn N, Jeon I, Yoon J, et al. Carbon-sandwiched perovskite solar cell. *J Mater Chem A*. 2018;6(4):1382-1389. doi:10.1039/C7TA09174E
79. Fagiolari L, Bella F. Carbon-based materials for stable, cheaper and large-scale processable perovskite solar cells. *Energ Environ Sci*. 2019;12(12):3437-3472. doi:10.1039/C9EE02115A
80. Musumeci AW, Silva GG, Liu J-W, Martens WN, Waclawik ER. Structure and conductivity of multi-walled carbon nanotube/poly(3-hexylthiophene) composite films. *Polymer*. 2007;48(6):1667-1678. doi:10.1016/j.polymer.2007.01.027
81. Lee C, Lee S-W, Bae S, et al. Carbon nanotube electrode-based perovskite–silicon tandem solar cells. *Solar RRL*. 2020;4(12): 2000353. doi:10.1002/solr.202000353
82. Kim K, Lee S, Nam JS, et al. Highly transparent and mechanically robust energy-harvestable piezocomposite with embedded 1D P(VDF-TrFE) nanofibers and single-walled carbon nanotubes. *Adv Funct Mater*. 2023;33(14):2213374. doi:10.1002/adfm.202213374
83. Zai H, Zhang D, Li L, et al. Low-temperature-processed inorganic perovskite solar cellsviasolvent engineering with enhanced mass transport. *J Mater Chem A*. 2018;6(46):23602-23609. doi:10.1039/C8TA09859J
84. Wang J, Chen L, Qian Z, Ren G, Wu J, Zhang H. Optimal intermediate adducts regulate low-temperature $CsPbI_2Br$ crystallization for efficient inverted all-inorganic perovskite solar cells. *J Mater Chem A*. 2020;8(47):25336-25344. doi:10.1039/D0TA07663E

85. Kim K, Han J, Lee S, et al. Liquid-state dithiocarbonate-based polymeric additives with monodispersity rendering perovskite solar cells with exceptionally high certified photocurrent and fill factor. *Adv Energy Mater*. 2023;13(14):2203742. doi:10.1002/aenm.202203742
86. Zarazua I, Bisquert J, Garcia-Belmonte G. Light-induced space-charge accumulation zone as photovoltaic mechanism in perovskite solar cells. *J Phys Chem Lett*. 2016;7(3):525-528. doi:10.1021/acs.jpclett.5b02810
87. Parida B, Yoon S, Ryu J, Hayase S, Jeong SM, Kang D-W. Boosting the conversion efficiency over 20% in $MAPbI_3$ perovskite planar solar cells by employing a solution-processed aluminum-doped nickel oxide hole collector. *ACS Appl Mater Interfaces*. 2020;12(20):22958-22970. doi:10.1021/acsami.0c04618

SUPPORTING INFORMATION

Additional supporting information can be found online in the Supporting Information section at the end of this article.

How to cite this article: Yoon S, Lee IH, Han J, et al. Semi-transparent metal electrode-free all-inorganic perovskite solar cells using floating-catalyst-synthesized carbon nanotubes. *EcoMat*. 2024;6(3):e12440. doi:10.1002/eom2.12440